Available online at www.sciencedirect.com
ScienceDirect
International Journal of Heat and Fluid Flow 28 (2007) 1379–1390
International Journal of HEAT AND FLUID FLOW
www.elsevier.com/locate/ijhff

Simulation of wing-body junction flows with hybrid RANS/LES methods

Song Fu *, Zhixiang Xiao, Haixin Chen, Yufei Zhang, Jingbo Huang

School of Aerospace Engineering, Tsinghua University, Beijing 100084, China

Received 17 December 2006; received in revised form 9 May 2007; accepted 11 May 2007
Available online 9 July 2007

Abstract

In this paper, flows past two wing-body junctions, the Rood at zero angle of attack and NASA TN D-712 at 12.5° angle of attack, are investigated with two Reynolds-Averaged Navier-Stokes (RANS) and large eddy simulation (LES) hybrid methods. One is detached eddy simulation (DES) and the other is delayed-DES, both are based on a weakly nonlinear two-equation k–ω model. While the RANS method can predict the mean flow behaviours reasonably accurately, its performance for the turbulent kinetic energy and shear stress, as compared with available experimental data, is not satisfactory. DES, through introducing a length scale in the dissipation terms of the turbulent kinetic energy equation, delivers flow separation, a vortex or the onset of vortex breakdown too early. DDES, with its delayed effect, shows a great improvement in flow structures and turbulence characteristics, and agrees well with measurements.

Keywords: Wing-body junction; RANS/LES hybrid methods; Weakly nonlinear k–ω model

1. Introduction

Junction flow occurs when a boundary layer encounters an obstruction. It is a generic process in numerous aerodynamic and hydrodynamic configurations, such as the wing-fuselage junction of aircraft, the appendage-hull junction of submarine, the blade-hub assemblies of turbines, and so on. For wing-body junction flow at reasonably large Reynolds number, the adverse pressure gradient in the streamwise direction imposed by the wing often causes the upwind boundary layer on the body to separate and form multiple horseshoe vortices around the wing. The primary horseshoe vortex can demonstrate a large-scale low-frequency bistable unsteadiness which appears to be generated in the nose region and may lead to the generation of undesired noise. Some relatively weak, unsteady secondary vortices, which energize the low-momentum flow in the corner of the junction and decrease the tendency to separation (Apsley and Leschziner, 2001), are also generated very close to the wing base.

Recently, wing-body junction flows in flight vehicle configurations have received much attention. Straight wing, which is perpendicular to the fuselage, is likely to cause a large separation region near the junction where the fuselage boundary layer encounters the strong pressure rise of the wing stagnation region. Better understanding and accurate prediction of the junction flows can effectively help the design of lower drag and high-efficiency flight vehicles. The wing-body junction flow is well known for being rich in flow physics. The flow is highly strained, anisotropic, and strongly affected by unsteady turbulent transport. It thus poses a great challenge to turbulence-modeling researchers.

For the experimental studies, the case with flow passing a 3:2 elliptical nose and a NACA 0020 tail model (Devenport and Simpson, 1990; Simpson, 2001), commonly named Rood wing-body junction, investigated by Simpson's group (Simpson, 2001) is perhaps best known. Significant amount of modeling work have been carried out in the past decade (e.g. Chen, 1995; Fu et al., 1997b; Parneix

* Corresponding author. Tel./fax: +86 10 6277 9215.
E-mail address: fs-dem@tsinghua.edu.cn (S. Fu).

0142-727X/$ - see front matter © 2007 Elsevier Inc. All rights reserved.
doi:10.1016/j.ijheatfluidflow.2007.05.007

et al., 1998; Apsley and Leschziner, 2001; Jones and Clarke, 2005) aiming to capture this important flow numerically. Chen's study (1995) examined the performance of a two-layer k–ε eddy-viscosity model and a low-Re-extension of the high-Re second-moment closure. The second-moment closure model is able to capture the detached spiraling motion and gives a more rational representation of the transverse turbulence structure. Fu et al.'s study (1997b) focused on the performance of quadratic eddy-viscosity formulations. Their results presented some improvement in modeling shear stress in the vortex. Parneix et al.'s study (1998) obtained favorable results for the velocity and turbulence energy with the "V2f" model. Apsley and Leschziner's work (2001) presented relatively comprehensive computation results with twelve turbulence models, including five linear, three nonlinear eddy-viscosity, and four Differential Reynolds-Stress Models (DRSM). The main findings of the study were that DRSM offered predictive advantages over the other models examined, especially in terms of the far-field structure of the horseshoe vortex, although no model achieved close agreement with the experimental data with respect to both mean flow and turbulence quantities. Jones and Clarke's study (2005) showed some numerical results using the Fluent commercial software with several turbulence models, including the renormalized k–ε model, the DRSM, the V2f model, the Spalart and Allmaras (1992) model and the k–ω SST (shear stress transport) model proposed by Menter (1994). That study suggested that the V2f model could offer the best combination of computational accuracy, efficiency and ease of use. Franke et al. (2005) employed two explicit algebraic Reynolds stress models for the transonic transport configurations, including both generic and DLR F4 wing-body junctions. Xiao et al. (2005) predicted the interference flows past the NASA TN D-712 wing-body standard model (briefly called TN D-712) at high angles of attack with a low-Re two-equation k–g model which requires no parameterization of the distance to the wall.

Although, the geometry of a wing-body junction is relatively simple, the flow physics are so complex that the Reynolds-Averaged Navier-Stokes (RANS) method with turbulence modelling could not reliably provide satisfactory agreement with the measurements. The RANS methods had been developed to predict many of the important phenomena in complex vortical flows, but it was not intended to simulate the large-scale *unsteady* vortex structures along the wing. Large eddy simulation (LES) is a powerful tool for resolving the large, energy-containing scales of motion that are typically dependent of geometry and boundary conditions. The small scale motion is nearly homogeneous and is treated with sub-grid scale models in LES. However, when LES is applied to boundary layers, the overall computational cost does not differ significantly from that of direct numerical simulation. The "large eddies" close to the solid wall are physically small in scale. A semi-empirical application is required in the treatment of high Reynolds number boundary layer.

To make the best use of RANS and LES, an alternative modeling strategy of turbulent flows, often called the hybrid RANS/LES method, has recently been proposed to predict the unsteady and geometry-dependent separating flows. Such hybrid methods combine a high-efficiency turbulence model near the wall, where the flow is dominated by small scale motion, with an LES-type treatment for the large-scale motion in the flow region far away from the wall. The well-known and wide-used RANS/LES approach, named as detached eddy simulation (DES, Spalart et al., 1997), was proposed by Spalart about a decade ago. Later, Strelets (2001) proposed a DES-type hybrid method based on the SST model through introducing a length scale L_t in the turbulent kinetic energy transport equation. Menter and Kuntz (2003) developed a delayed-DES method based on the SST model, which acts as the RANS model near the wall and prevents the pre-switching from RANS to LES due to the locally refined grids. Sparlart et al. (2006) extended the delayed-DES for any turbulence models with eddy-viscosity, including the fundamental S-A model.

The core idea of the hybrid methods is to combine RANS near the wall with LES in the separation region. The fundamental turbulence models still significantly affect the predicted flow characteristics for aircraft application. To construct the hybrid RANS/LES methods rationally, it is generally hoped that the turbulence model has good numerical properties and has a *low Reynolds number* capability to resolve the near-wall turbulence characteristics. The two-equation k–ω model, for its favorable numerical aspects, is commonly taken as an appropriate choice even though the original version proposed by Wilcox (1988) suffers from undesirable freestream-dependence. The SST model is a hybrid approach through coupling the k–ω model in the near-wall region with the less freestream-dependent k–ε model outside the boundary layer. This model considers the transport of the principal turbulent shear stress and shows a good capability for modeling adverse pressure gradients flows. Nonlinearity in eddy-viscosity modeling had been reconsidered in the view of realizability, which is regrettably violated by most of the linear eddy-viscosity formulations based on Boussinesq assumption (Fu et al., 1997a). But, it is found that weakly nonlinear eddy-viscosity formulations, based on Wilcox's k–ω model with three-dimensional Durbin's correction (referred to as the WD+ model, Durbin, 1996), can effectively further improve the model's performance under adverse pressure gradients, especially for flows with shock-wave/boundary layer interaction (Soo and Jang, 2004).

In this article, the performance of the WD+ model is further explored in flows around wing-body junctions in flight vehicle configuration. Hybrid approaches, including DES and delayed-DES methods based on the WD+ model, are employed to capture the complex vortex physics and the chaotic nature of the flow around Rood and TN D-712 wing-body junctions. It is hoped that this study will lead to better understanding of the complex flows around aircraft geometry with different components.

2. Turbulence models and hybrid RANS/LES methods

In the present work, the k–ω family turbulence models are considered, and C_μ is incorporated into the definition of ω.

2.1. Wilcox's k–ω model

The original k–ω model developed by Wilcox is given as

$$\frac{\partial \rho k}{\partial t}+\frac{\partial \rho u_j k}{\partial x_j}=\frac{\partial}{\partial x_j}\left((\mu+\sigma_k\mu_t)\frac{\partial k}{\partial x_j}\right)+\tau_{ij}S_{ij}-\beta^*\rho k\omega \quad (1)$$

$$\frac{\partial \rho \omega}{\partial t}+\frac{\partial \rho u_j \omega}{\partial x_j}=\frac{\partial}{\partial x_j}\left((\mu+\sigma_\omega\mu_t)\frac{\partial \omega}{\partial x_j}\right)+\gamma\frac{\omega}{k}\cdot(\tau_{ij}S_{ij})-\beta\rho\omega^2 \quad (2)$$

where $\tau_{ij}=2\mu_t(S_{ij}-S_{kk}\ \delta_{ij}/3)-2\rho k\delta_{ij}/3$ is the Reynolds-stress tensor modeled with the Boussinesq eddy-viscosity hypothesis; S_{ij} is the strain rate defined as $(\partial u_i/\partial x_j+\partial u_j/\partial x_i)/2$. The constants are $\sigma_k=\sigma_\omega=0.5$, $\gamma=5/9$, $\beta^*=0.09$ and $\beta=3/40$. The linear eddy-viscosity is defined as

$$\mu_{t,\mathrm{Wilcox}}=\rho k/\omega \quad (3)$$

Eq. (3) was originally designed to predict accurately the boundary layer flows with zero pressure gradient.

2.2. The k–ω–WD+ model

The linear eddy-viscosity definition in Eq. (3) is known to be inadequate in the prediction of flow under adverse pressure gradients. The weakly nonlinear correction is proposed to produce asymptotic behavior of C_μ when S_{ij} approaches infinity. In the WD+ model, the equations remain the same as those in the original Wilcox's version. A new formulation of eddy-viscosity μ_t with a weakly nonlinear correction is defined as:

$$\mu_{t,\mathrm{WD+}}=\min\left[\frac{\rho k}{\omega};\frac{\rho a_1 k}{\sqrt{(\Omega^2+\tilde{S}^2)/2}}\right] \quad (4)$$

where $a_1=0.31$, $\tilde{S}^2=2(S_{ij}-\delta_{ij}S_{ll}/3)(S_{ji}-\delta_{ji}S_{kk}/3)$ and Ω is the magnitude of the vorticity defined as $\Omega=\sqrt{2W_{ij}W_{ij}}$ with $W_{ij}=(\partial u_i/\partial x_j-\partial u_j/\partial x_i)/2$ denoting the rate of rotation tensor.

2.3. The shear stress transport model (SST)

This model also adopts Wilcox's k–ω model, which is well behaved near solid walls and needs no low Reynolds number corrections. At the same time, it combines with the standard k–ε model (reformulated in a k–ω style), which is relatively insensitive to free-stream values in the outer edge of the boundary layer and free-stream. The switching is realized by a flow dependent blending function. The SST model also limits the eddy-viscosity by forcing the turbulent shear stress to be bounded by constant times the turbulent kinetic energy inside boundary layers (a realizability constraint). This modification improves the model's performance on flows with strong adverse pressure gradients and separation.

Mathematically, the SST turbulence model equations adopt the same k-equaiton, Eq. (1), as in the Wilcox's k–ω model, but the ω equation is given as:

$$\frac{\partial \rho \omega}{\partial t}+\frac{\partial \rho u_j \omega}{\partial x_j}=\frac{\partial}{\partial x_j}\left((\mu+\sigma_\omega\mu_t)\frac{\partial \omega}{\partial x_j}\right)+\gamma\frac{\omega}{k}\cdot(\tau_{ij}S_{ij})-\beta\rho\omega^2+2(1-F_1)\frac{\rho\sigma_{\omega 2}}{\omega}\frac{\partial k}{\partial x_j}\frac{\partial \omega}{\partial x_j} \quad (5)$$

Here, the blending function F_1 is defined as

$$F_1=\tanh\left\{\left[\min\left(\max\left(\frac{\sqrt{k}}{0.09\omega d};\frac{500\mu}{\rho d^2\omega}\right);\frac{4\rho\sigma_{\omega 2}k}{CD_{k\omega}d^2}\right)\right]^4\right\} \text{ with}$$

$$CD_{k\omega}=\max\left(\frac{2\rho\sigma_{\omega 2}}{\omega}\frac{\partial k}{\partial x_j}\frac{\partial \omega}{\partial x_j};10^{-20}\right). \quad (6)$$

Here, d refers to the distance from the nearest wall. Some other constants are calculated from $\phi=F_1\phi_1+(1-F_1)\phi_2$, where the ϕ's are the constants: $\sigma_{k1}=0.85$, $\sigma_{\omega 1}=0.5$, $\beta_1=0.075$, $\gamma_1=\beta_1/\beta^*-\sigma_{\omega 1}\kappa^2/\sqrt{\beta^*}=0.553$; $\sigma_{k2}=1.0$, $\sigma_{\omega 2}=0.856$, $\beta_2=0.0828$, $\gamma_2=\beta_2/\beta^*-\sigma_{\omega 2}\kappa^2/\sqrt{\beta^*}=0.44$ and $\kappa=0.41$.

The eddy-viscosity coefficient in SST model is defined as

$$\mu_{t,\mathrm{SST}}=\min\left(\frac{\rho k}{\omega};\frac{\rho a_1 k}{\Omega F_2}\right) \quad (7)$$

where F_2 is another blending function defined as

$$F_2=\tanh\left\{\left[\max\left(2\frac{\sqrt{k}}{0.09\omega d};\frac{500\mu}{\rho d^2\omega}\right)\right]^2\right\}. \quad (8)$$

Both F_1 and F_2 in SST model are equal to one near the wall while they approach to zero in the freestream out of the boundary layer.

In Eq. (7), the eddy-viscosity in SST model is similar in a form to Eq. (4) but also includes nonlinear effect. Therefore, the SST model can be thought as a weakly nonlinear turbulence model, too.

2.4. DES and DDES methods

The motivation of the hybrid RANS/LES method is to combine the best features of both the LES and RANS methods. RANS can predict attached flows well with relatively few computational costs. LES has demonstrated its ability to resolve separated flows satisfactorily but with higher computational cost for boundary layer flows. In the RANS/LES hybrid approach, the Reynolds-stress or sub-grid stress tensor is defined as:

$$\tau_{ij}=-\overline{\rho u_i' u_j'} \quad (9)$$

where u_i' denotes the fluctuating velocity u-component and the over-bar represents the mean or large-scale value. The stress tensor in DES and DDES is modeled with the LES-type Smagorinsky model, i.e.

$$\tau_{ij} = 2\rho\nu_{\mathrm{Sma}}S_{ij}, \quad \nu_{\mathrm{Sma}} = C_{\mathrm{S}}\Delta^2\widetilde{S} \tag{10}$$

where C_s is the model constant ranging from 0.01 to 0.05 and Δ is the grid length scale.

To construct a DES-type hybrid method based on two-equation models, some transformation is adopted for the dissipation term in the turbulent kinetic energy transport equation. After introducing a length scale, Eq. (1) can be written as

$$\frac{\partial(\rho k)}{\partial t} + \frac{\partial \rho u_j k}{\partial x_j} = \frac{\partial}{\partial x_j}\left((\mu + \sigma_k\mu_t)\frac{\partial k}{\partial x_j}\right) + \tau_{ij}S_{ij} - \beta^*\rho k\omega F_{\mathrm{DES}} \tag{11}$$

where F_{DES} is the hybrid function defined as

$$F_{\mathrm{DES}} = \max\left[(1 - F_{\mathrm{SST}})\cdot\frac{L_{\mathrm{t}}}{C_{\mathrm{DES}}\Delta};1\right]; \tag{12}$$

the turbulence length scale L_{t} is defined as $L_{\mathrm{t}} = k^{1/2}/(\beta^*\omega)$; $C_{\mathrm{DES}} = 0.78$; Δ is the grid scale defined as $\Delta = \max(\Delta x, \Delta y, \Delta z)$; F_{SST} can be taken as 0, F_1 or F_2, where F_1 and F_2 are the two blending functions in the SST model. If $F_{\mathrm{SST}} = 0$, the hybrid method reverts to a Strelets-type DES method. If $F_{\mathrm{SST}} = F_1$ or F_2, then, this hybrid approach is called the delayed-DES method. Due to the numerical properties of F_1 and F_2, (1-F_{SST}) approaches zero near the wall and the DDES will act in the RANS mode. At the same time, (1-F_{SST}) becomes zero out of the boundary layer and the DDES goes to the original Strelets' DES model. Therefore, the delayed-DES can ensure itself to act in the RANS mode near the wall without the effects on the locally clustered grid scales. In other words, this hybrid method can delay the switching from RANS to LES near the wall due to the grid scales, especially the locally refined grids in the streamwise and spanwise direction for the complex aircraft configurations. In this paper, F_{SST} is taken as F_2.

The ω-equation and the eddy-viscosity definition are the same as that in the WD+ or Wilcox's model.

In the Strelets-type DES method (i.e. $F_{\mathrm{SST}} = 0$), when $L_{\mathrm{t}}/(C_{\mathrm{DES}}\Delta) < 1$, then $F_{\mathrm{DES}} = 1$, the hybrid method acts in the RANS mode; When $L_{\mathrm{t}} > C_{\mathrm{DES}}\Delta$, the method acts in the Smagorinsky LES mode. When turbulence production is balanced by the dissipation term, $P_k = \rho\nu_{\mathrm{t}}\tilde{S}^2 = D_k = \rho k^{3/2}/L_{\mathrm{t}}, k = \beta^* L_{\mathrm{t}}^2\tilde{S}^2$ and $L_{\mathrm{t}} = C_{\mathrm{DES}}\Delta$. Then the eddy-viscosity can be rewritten as

$$\nu_{\mathrm{t}} = (\beta^*)^{3/2}(C_{\mathrm{DES}}\Delta)^2\tilde{S} \propto \Delta^2\tilde{S} \tag{13}$$

From Eq. (10), the eddy-viscosity is similar as that of Smagorinsky's model. When the grid is locally refined, the hybrid method will act as in a LES mode.

3. Numerical methods

The computations here are all based on a compressible solver using a Roe (1981) flux-difference splitting scheme with a 3rd order monotone upstream scheme for conservation laws and a Radespiel and Swanson (1991) entropy fix in a cell-centered finite-volume formulation. A modified fully implicit lower–upper symmetric Gaussian Seidel (LU-SGS, Yoon and Jameson, 1987; Xiao et al., 2006) model with Newton-like sub-iteration in pseudotime is taken as the time marching method when solving the mean flow and the turbulence model equations. Global non-dimensional time stepping is implemented to capture the unsteady properties of the separation flows. It indicates that the RANS method here is the unsteady-RANS type. Implicit residual smoothing is employed to accelerate convergence in the sub-iterations. The approach is parallelized using domain-decomposition and message-passing-interface (MPI) strategies for the platform on PC clusters with 64-bit AMD Athlon 3000+.

For the Rood case, the detailed boundary conditions are described in the following section. For the TN D-712 case, at far-field boundaries, the 1D Riemann characteristic analysis is employed to construct a non-reflecting boundary condition. For smooth surfaces, no-slip boundary condition is used. Symmetric boundary condition is applied for its half-model. For computational convenience, "Ghost cells" are used to treat all kinds of boundary conditions including the boundary of the adjacent zonal domains.

The turbulent kinetic energy and specific dissipation rate transport equations are solved, decoupled from the mean flow equations, using the LU-SGS method. The production terms are treated explicitly, lagged in time while the dissipation and diffusion terms are treated implicitly (they are linearized and a term is brought to the left-hand-side of the equations). Treating the dissipation terms implicitly helps increase the diagonal dominance of the left-hand-side matrix. The advective terms are discretized using second-order upwind scheme. The diffusive terms are discretized using a second-order central scheme.

In the present work, the coordinate x denotes the streamwise direction, z the spanwise direction and y the direction normal to the symmetric plane. For the Rood junction, the maximum thickness (T) of the wing is chosen as the characteristic length; for the TN D-712 junction, the half-span ($B/2$) is chosen as the characteristic length. The grids are generated by solving elliptic equations. Appropriate zonal decomposition and grid topology selection are performed according to the features of the configuration. To investigate the performance of the weakly nonlinear WD+ model, separated flow with horseshoe vortices past the Rood junction is computed first. The numerical results by the SST model are also presented for comparison. The initial conditions for the two hybrid methods are obtained by solving the RANS equations based on the WD+ model. The unsteady-RANS, DES and DDES methods are then

solved for wing-body junction flows past the Rood and the TN D-712.

4. Results and discussion

4.1. Rood junction

For Rood junction the wing section includes a 3:2 semi-elliptic nose and a NACA 0020 tail. The Reynolds number is 115,000. The wing chord is 4.254. The inlet conditions are fixed and prescribed at $x/T = -18.24$ using the experimental measurements from the ERCOFTAC database. The outflow boundary is at $x/T = 16$ with zero streamwise gradients. The boundaries at $y/T = 0$, $y/T = 7$ and $z/T = 3$ are assumed to be symmetric. No-slip conditions are applied at the wall.

Fig. 1 presents the grids around the Rood junction. Two block grids, one of $140 \times 60 \times 80$ cells and the other of $40 \times 60 \times 25$ cells (about 0.7 million cells), are generated to cover only half of the symmetric wing. The minimum cells height near the walls is about 1.0635×10^{-4}.

Many numerical researches have mainly focused on the horseshoe vortex patterns ahead of the wing nose. In this paper, results at five typical planes (shown in Fig. 2) including the upwind symmetric plane ($y/T = 0$), planes at the maximum thickness ($x/T = 0.76$), the middle wing ($x/T = 2.72$), the trailing edge ($x/T = 3.95$) and the wake ($x/T = 6.38$) are presented in detail.

4.1.1. Difference between SST and WD+ (RANS)

To investigate the performance of WD+ model, the widely-used SST model is also applied to validate the codes and to compare with the WD+ model. Fig. 3 presents comparisons on the streamwise velocity component (U/U_{ref}) and turbulent kinetic energy (k/U_{ref}^2) in the plane of symmetry with these two models. Comparisons are implemented at nine streamwise positions on the symmetric plane from $x/T = -0.461$ to -0.05. Small differences in the turbulent kinetic energy between the WD+ (denoted as the solid lines) and SST (denoted as the dashed lines) models occur. The WD+ model returns only marginally better turbulence energy distribution at $x/T = -0.251$ than that of SST model. The difference in the velocity u-components is unnoticeable.

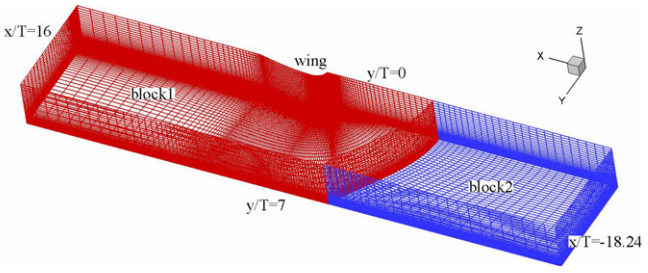

Fig. 1. Grids around rood junction.

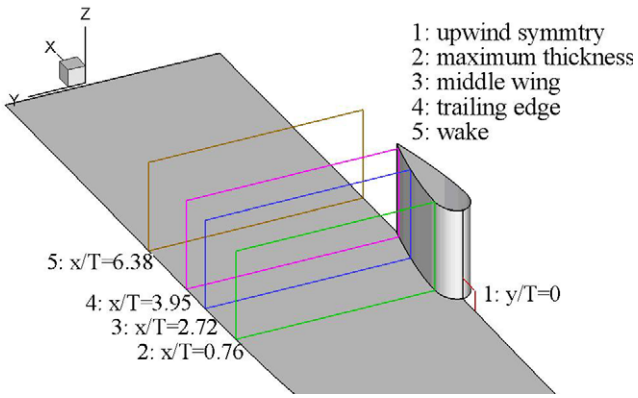

Fig. 2. The position of the measurement plane.

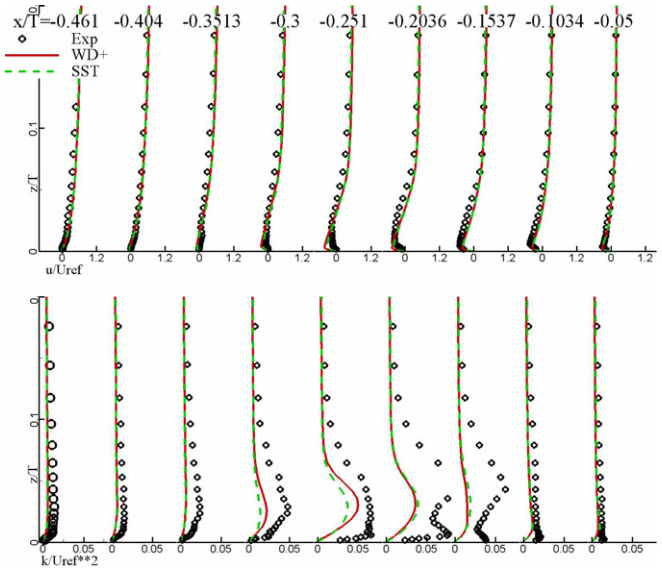

Fig. 3. Comparisons on U and k with the WD+ and SST.

4.1.2. Difference on grid (RANS)

A finer grid mesh, consisting of $140 \times 65 \times 100$ and $40 \times 65 \times 25$ cells (totaling about 1.0 million cells), is employed to test the effects on the grid density. The numerical results about the u-velocity and turbulence kinetic energy with the WD+ model demonstrate that little difference exists between the grid meshes of 0.7 and 1.0 million cells (see Fig. 4). Therefore, the following computations are all based on the grids which consist of 0.7 million cells. Although, the 40% strong increase in the grid density in a three dimensional problem is not convincing for the purpose of testing grid independence, grid density is increased in the spanwise and normal direction of the wing to make the effective use of the limited number of grid points.

4.1.3. Flowfields on the symmetric plane ($y/T = 0$)

Fig. 5 presents the horseshoe vortex and velocity vectors on the symmetric plane ahead of the wing. The horseshoe vortex is observed in the experiment at about $x/T = -0.20$ before the wing nose. The RANS and DDES present

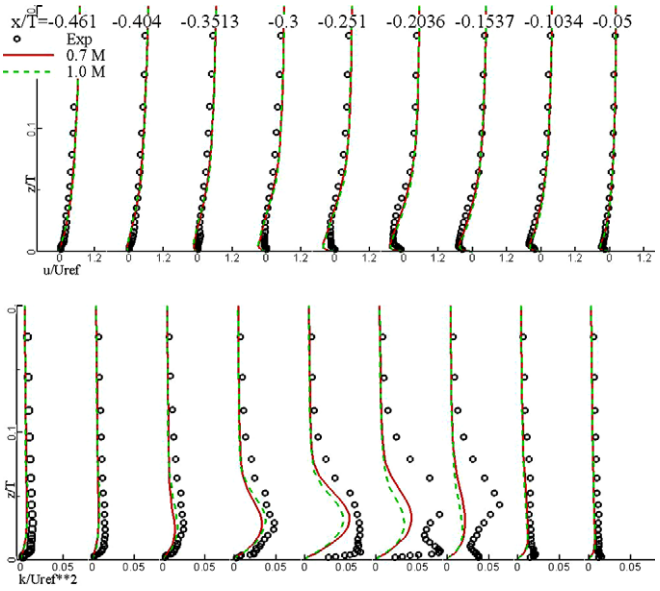

Fig. 4. Comparisons on U/U_{ref} and k/U_{ref}^2 based on two grids.

velocity vectors similar with the measurements while the primary horseshoe vortex given by DES is somewhat too far upwind. The DES and DDES results have been obtained with time averaging procedure. The velocity profiles for the streamwise and spanwise components are also given in Fig. 5. Due to limitations of the measurement facilities, measurement close to the wing base is unavailable. It is seen there from the numerical results that even the tertiary vortices can be observed. The intensity and extent of the secondary vortex with RANS is a little larger than those with the hybrid methods. Due to the too far upwind vortex, DES shows that the profiles of velocity have distinct differences from those of the measurements and other numerical results. RANS and DDES present a more satisfactory agreement with the experimental velocity profiles.

Although, the RANS (the dashed lines) demonstrates satisfactory results for flow structures, it delivers much smaller levels in the turbulent kinetic energy and the shear stress than those in the experiments (Fig. 6). Since, the spanwise normal stresses were not measured on the symmetry plane it is roughly estimated as $\overline{vv} = 0.5(\overline{uu} + \overline{ww})$ following Apsley and Leschziner (2001). The kinetic energy computed by Parneix et al. (1998) using v2f model at these nine streamwise positions are also plotted (shown as the dash-dot-dot line) in the same figure. But the v2f presents more satisfactory kinetic energy at $x/T = -0.2$ than those of WD+ model. At the other positions, its performance is similar with the WD+ model. DDES, in contrast, shows more satisfactory consistency with the experiments although some differences exist.

Comparisons on the turbulent shear stress contours in the plane of symmetry are presented in the Fig. 6. From these contours, only the DDES delivers the most similar results with the experiment. DES, which does not match the measurements, tends to separate too early. The WD+ model presents the relatively weaker shear stress distribution comparing with that of DDES. The shear stress contours with DRSM (Jakirlic) are referred to for comparison.

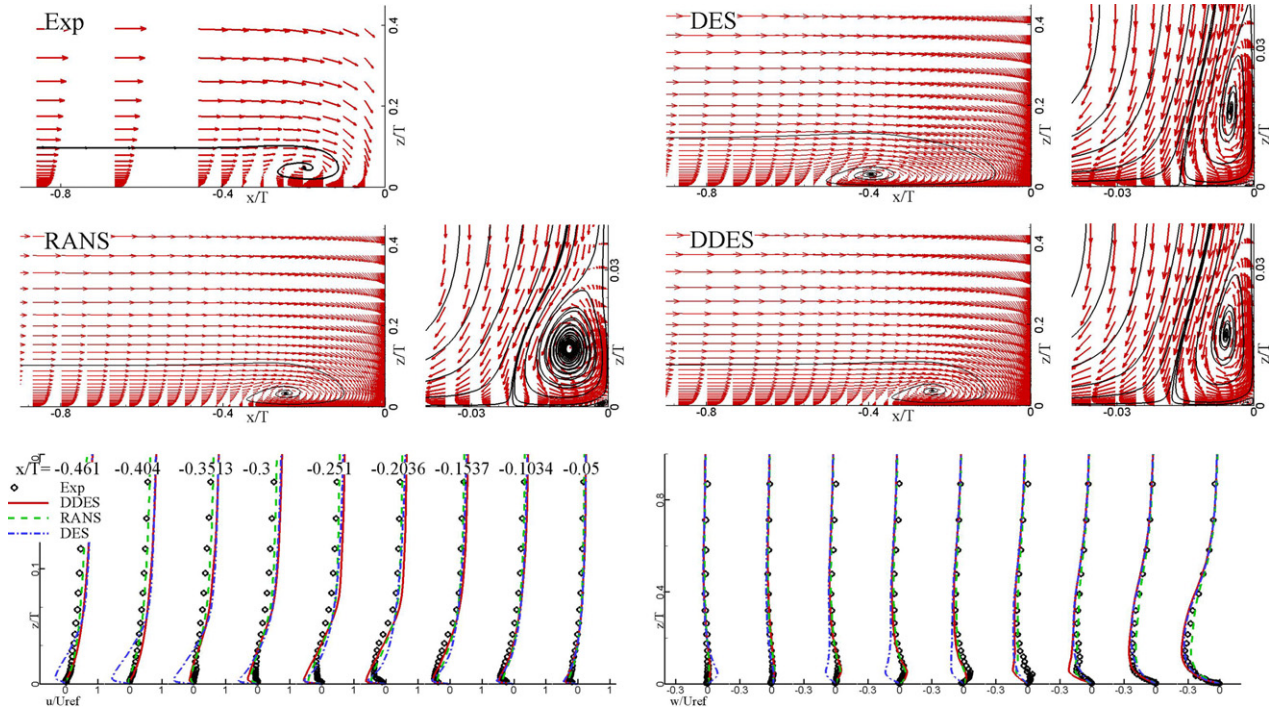

Fig. 5. Comparison of velocity vectors on the symmetric plane.

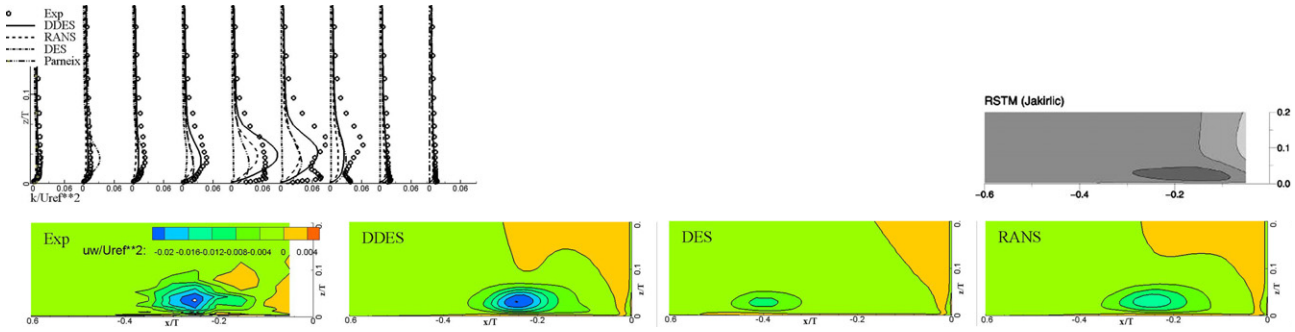

Fig. 6. The comparison on the turbulent kinetic energy and shear stress in the plane of symmetry.

4.1.4. Flow structures at three streamwise positions

The difference in the vortex structures upwind of the wing nose between the calculations and measurements is reflected further downstream as the resolved vortex evolves and develops along the wing-body junction. Fig. 7 shows the comparisons of cross-stream velocity profiles at Sections 2–4 (where $x/T = 0.76$, 2.72 and 3.95, respectively). All the numerical results match the measurements well except the DES results which exhibit more intense outward movement. The overall flow characteristics computed by DDES, including the vortices in the wake, the horseshoe vortex on the symmetric plane ahead of the wing base, and the flow patterns near the wing trailing edge, are shown in Fig. 8. As had been just discussed on the flow at the symmetry plane ahead of the wing, vortex development near the trailing edge and in the wake is equally important. From Fig. 8 it is seen that the flow recirculates near the trailing edge ($x/T = 3.95$) at the wing-plate junction. But the flow feature in the wake is basically dominated by the main horseshoe vortex. The turbulent kinetic energy and the cross-stream normal stress at the $x/T = 3.95$ plane are presented in Fig. 9. DDES gives the best agreement with the measurements while DES and RANS show somewhat large departure from the data.

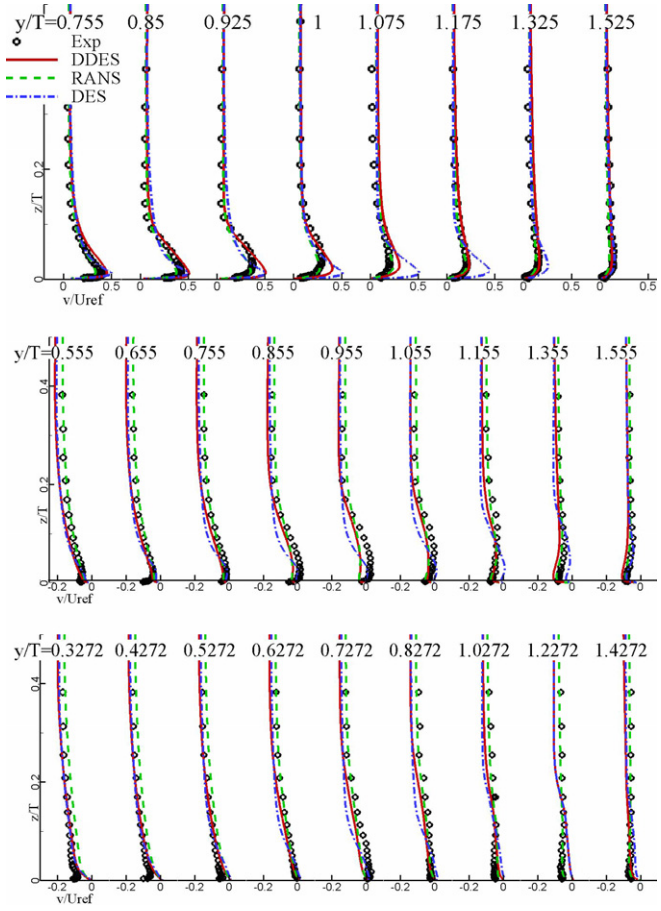

Fig. 7. Transverse velocity at different streamwise positions (maximum thickness, middle and trailing edge of the wing).

4.1.5. Flowfields in the wake (x/T=6.38)

The flowfields showing the turbulent kinetic energy and transverse flow structure in the wake at $x/T = 6.38$ are

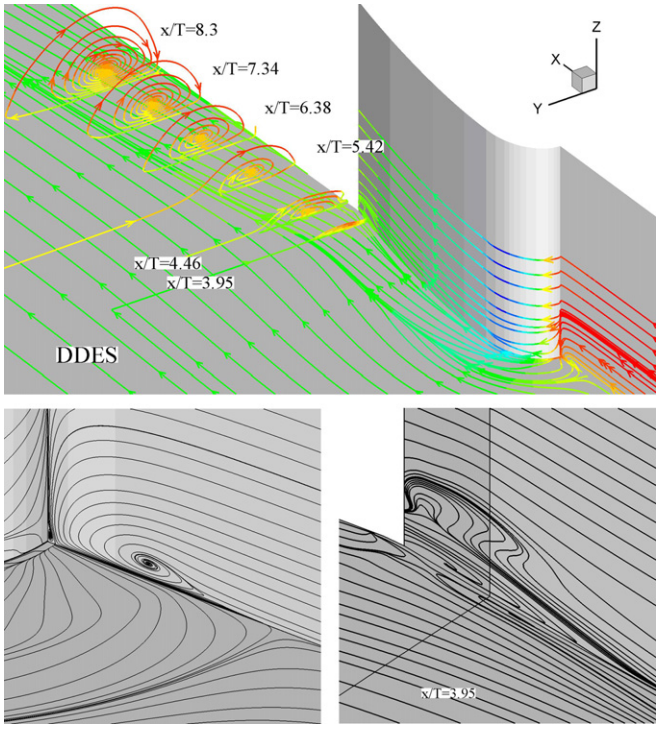

Fig. 8. flow patterns around the wing-body junction (a) shear stress lines and vortex in the wake; (b) upwind symmetry plane horseshoe vortex and (c) vortices near the trailing edge.

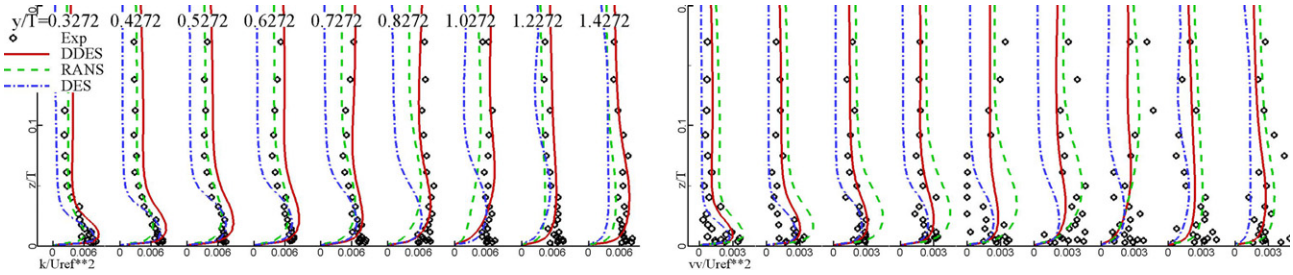

Fig. 9. Comparisons of turbulent kinetic energy and cross-streamwise normal stress near the trailing edge ($x/T = 3.95$).

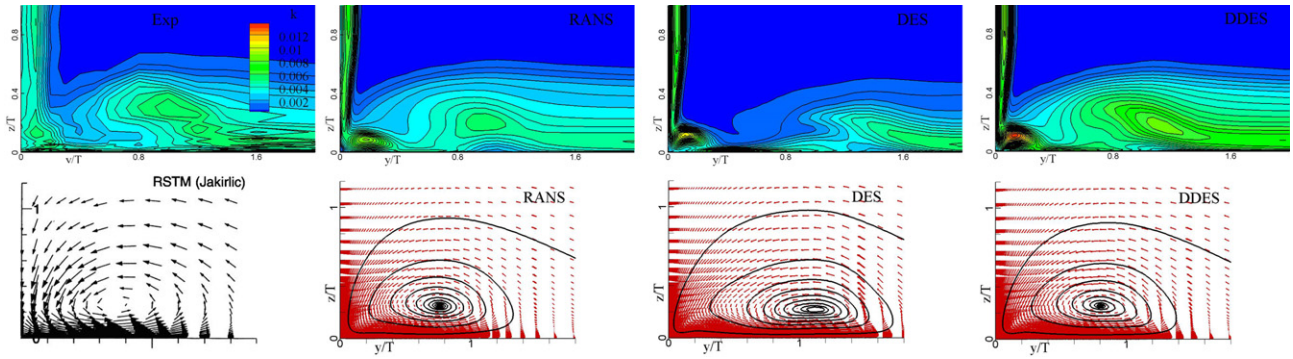

Fig. 10. Comparisons of turbulent kinetic energy and the vertical flow vectors in the wake ($x/T = 6.38$).

presented in Fig. 10 (there are no corresponding experimental data about velocity w, and the results computed by Apsley and Leschziner (2001) using the DRSM (Jakiric) model are employed for comparison). The figure shows the performance of the turbulence models through quantitative comparisons and qualitative differences in the vortical motion. There are evident difference in the predicted flow structure and intensity of the transverse motion.

The distribution and intensity of turbulent kinetic energy computed by DDES presents a very satisfactory agreement with those of the measurements. DES, however, shows the higher turbulent kinetic energy region far away from the symmetric plane. RANS presents similar results with those of DDES but with weaker turbulent kinetic energy. The velocity vectors by the RANS and DDES based on WD+ model are very similar with those computed by Apsley and Leschziner (2001).

The main vortex core coordinates on the symmetry plane ahead of the wing base and in the wake at $x/T = 6.38$ are presented in Table 1. It is seen there is little difference at the symmetry plane between RANS and DDES results, both can reasonably accurately predict the primary flow structure. DES, however, shows a relatively large departure from the measurements. In the wake, the core coordinates of the present RANS and DDES results are similar with those given by Apsley and Leschziner (2001).

It should be mentioned that all the DES and DDES results presented in this section are time-averaged.

Table 1
Comparisons on the vortex core coordinates

Plane	Methods	x/T	z/T
$Y/T = 0$	Exp	−0.199	0.0486
	RANS	−0.246	0.0335
	DES	−0.395	0.0297
	DDES	−0.243	0.0366
		y/T	z/T
$x/T = 6.38$	Apsley and Leschziner (2001)	$0.800 \pm 1\%$	$0.285 \pm 2\%$
	RANS	0.760	0.249
	DES	1.181	0.217
	DDES	0.804	0.254

4.2. TN D-712 junction

This wing-body configuration consists of a low aspect ratio, high swept angle thin mid-wing and a fuselage with pointed nose and boattailing afterbody. In the present work, five computational blocks with H-H type grids (about 2.0 million cells in the whole field, designated as Grid A) are employed with each block consisting of $160 \times 90 \times 27$ cells (shown in Fig. 12). To allow the delayed effects associated with the limiter (1-F_{SST}) in the DDES it is found necessary to locally refine the grids in the streamwise direction at the leading edge of the wing. Thus, 10 more grids are added in the so-called Grid B which in total includes $5 \times 170 \times 90 \times 27$ cells (about 2.2 million cells). The only difference between Grid A and B is in the grid density near the leading edge. As seen in Fig. 11, 11 and

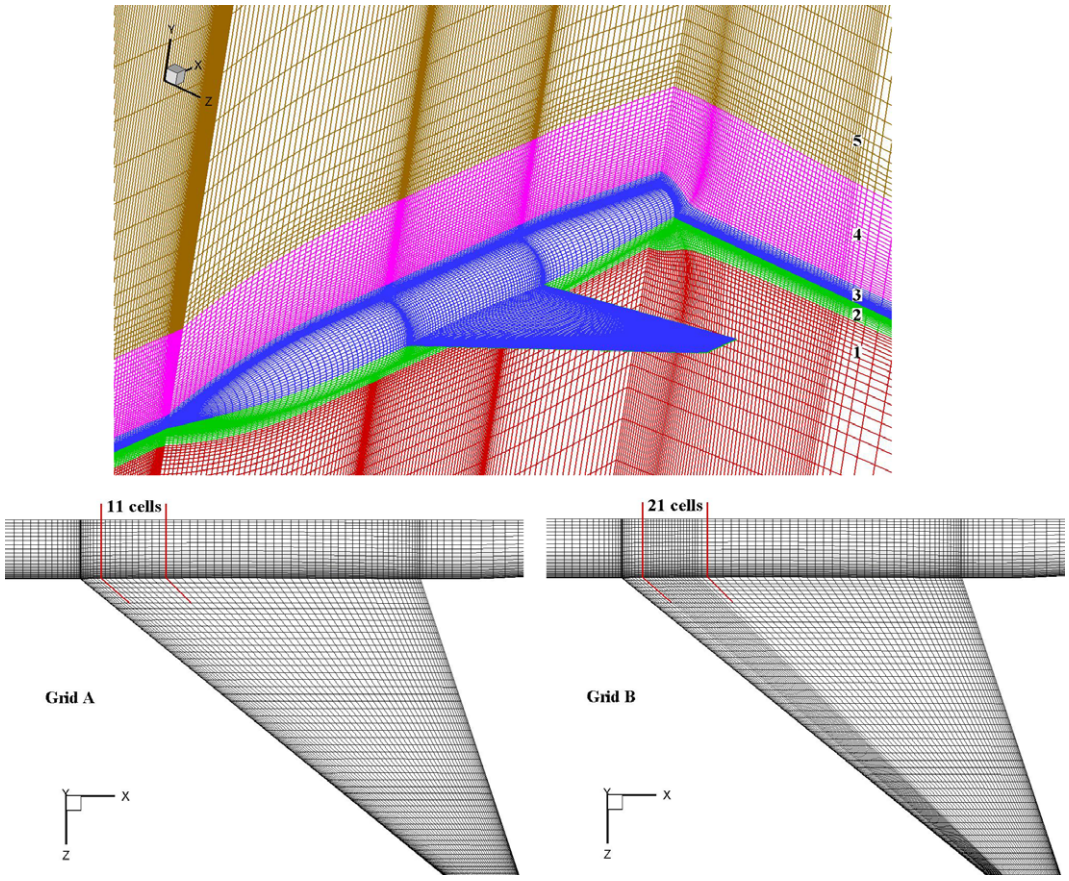

Fig. 11. Grids around TN D-712 Wing-fuselage junction.

21 grid points are located in the region between $2x/B = 1.59$ and 1.78 of Grid A and B, respectively.

The computations are performed for the Mach number 0.9 case; the Reynolds number is 7.5×10^6 (based on half-span) and the angle of attack is 12.5°. Different from the flow past the Rood junction at zero angle of attack, the flow around TN D-712 at this middle angle of attack exhibits understandably asymmetric patterns between the leeward and forward sides of the wing.

Again, many of the results for TN D-712 are time-averaged unless specially specified.

The computational pressure coefficients over the wing are compared with experimental data in Fig. 12. Three wing sections near the junction at $2z/B = 16$, 25 and 40% are presented. Especially, the section at $2z/B = 16\%$ is just at the wing-fuselage junction. Very strong aerodynamic interactions between the wing and fuselage can be found through the pressure distribution of wing root sections. At sections $2z/B \geqslant 60\%$ (though the results are not presented here), the flow is completely separated, and the pressure coefficients computed with all the turbulence models considered in here demonstrate no difference from each

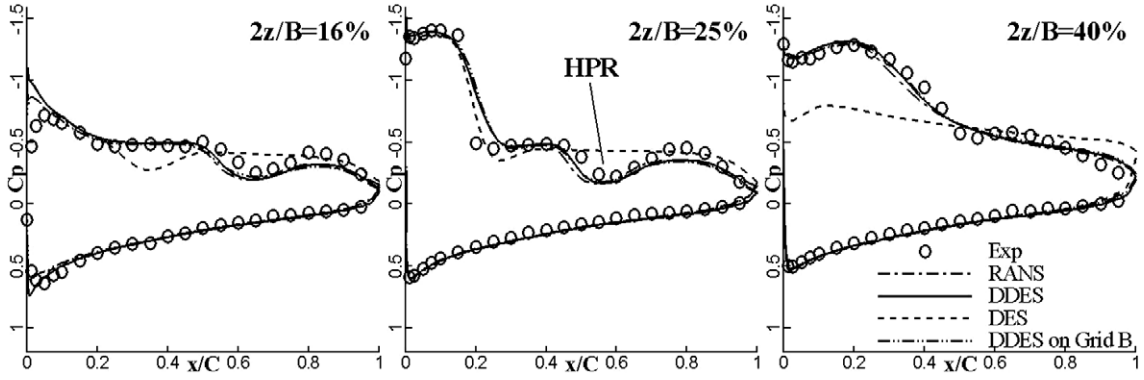

Fig. 12. Comparisons of pressure coefficients of different turbulence methods near the junction.

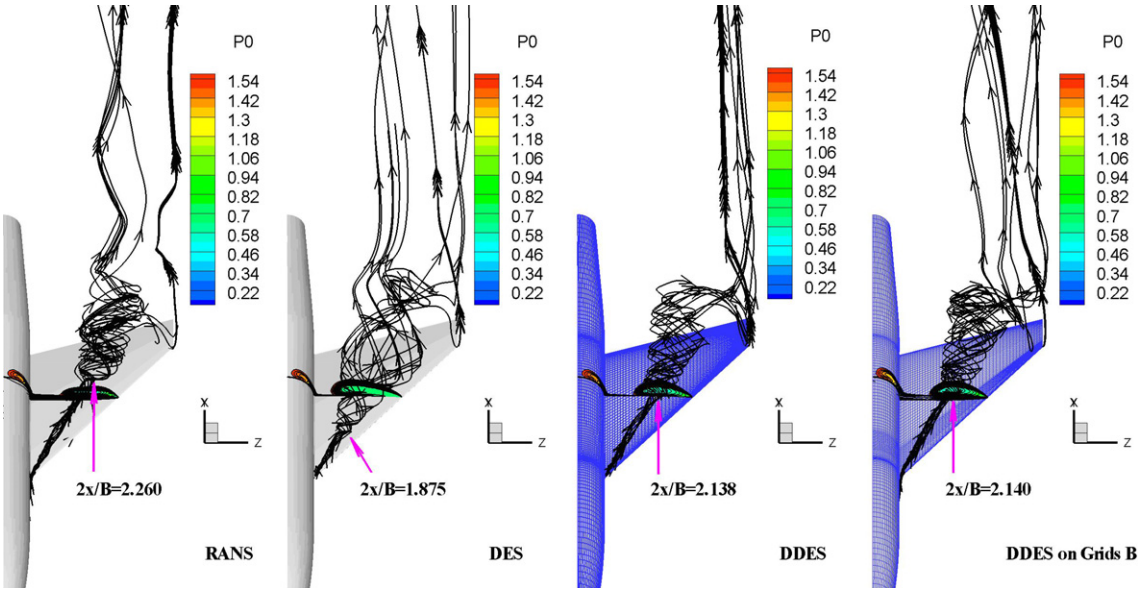

Fig. 13. Comparison on vortex over the wing with RANS, DES and DDES methods.

other. From Fig. 12, the wing surface pressure coefficients with RANS, DES and DDES models are all plotted. It is found that the results from Strelets-type DES show significant deviation from those of the measurements. The results obtained with RANS agree with the measurements and with DDES results surprisingly well despite of the vortex breakdown occurring at the leeward surface (Fig. 13). The reason can be attributed to the low-Re feature embedded in the WD+ model which delayed the breakdown of the wing-fuselage junction vortex. In the DES approach, turbulent length scale quickly over takes the grid spacing Δ causing the vortex to burst earlier.

From the study of flows around a 3D infinite span wing with strong adverse pressure, Menter and Kuntz (2003) pointed out that the original DES switching criterion affected the RANS mode and moved the separation point upstream relative to the original SST model and measurements. In the present study, with the analysis of vortices detached from the leading point of wing-fuselage conjunction (shown in Fig. 13), the main cause for the inaccuracy can also be identified as the original DES switching criterion, which pre-transfers from LES to RANS and moves the onset of the wing vortex breakdown far upstream (here, the onset of the wing vortex breakdown in the streamwise direction is at $2x/B = 1.875$ by DES and 2.260 by RANS, respectively). The negative influence of the DES-limiter on the RANS part of the hybrid methods is effectively reduced by DDES. The onset of the wing vortex breakdown by DDES is at $2x/B = 2.138$, just a little more upstream than that of the RANS. The onset of vortex breakdown at ($2x/B = 2.140$) based on Grid B does not differ from that of Grid A by DDES. It indicates that the DDES can effectively eliminate the influence of the locally refined grid scale. Differences on the baseline Grid A and the locally refined Grid B in the pressure coefficients, which are also plotted in Fig. 12, are insignificant for the DDES. Therefore, most of the computational results are based on Grid A.

Different to the mean flow behavior discussed so far, the instantaneous pictures of the flow from the RANS/LES hybrid calculations highlight the detachment of the vortices from the wing. Shown in Fig. 14 are four spanwise slices of the instantaneous vorticity contours over the wing at the angles of attack at 12.5° and 26.2°, respectively. At $2z/B = 0.25$ near the root of the wing at 12.5° angle of attack, flow is obviously attached to the wing surface as the vorticity contours are closely attached to the wall. In this case the RANS mode dominates the DDES computation. At the other sections of the same angle of attack, the vorticity contours display complex spatial variations over the wing suggesting the flow has detached from the wing surface. "Large eddies" and unsteady characteristics of the flow are predicted. The figure on the RHS of Fig. 14 has a much large angle of attack, 26.2°. Flow detachment from the wing surface occurs at the leading edge for all the spanwise sections shown in the figure starting almost from the wing root. Large eddies are obviously present in the flow.

Fig. 15 presents the transverse flow patterns of DDES results at four streamwise sections ($2x/B = 1.667$, 1.833, 2.167 and 2.500). Three anticlockwise detached vortices, including the fore-fuselage vortex, wing vortex from the leading point of the wing-fuselage conjunction and the horseshoe vortex close to the lower fuselage surface, are clearly illustrated. The total pressure contours are shown as the background color in these pictures. The most visible change in the streamwise direction is the shape and size of the wing vortex. At section $2x/B = 2.167$, the region of lower total pressure becomes large indicating breakdown occurred in the wing vortex. The horseshoe vortex is distinctly visible at $2x/B = 2.167$, while it almost disappears

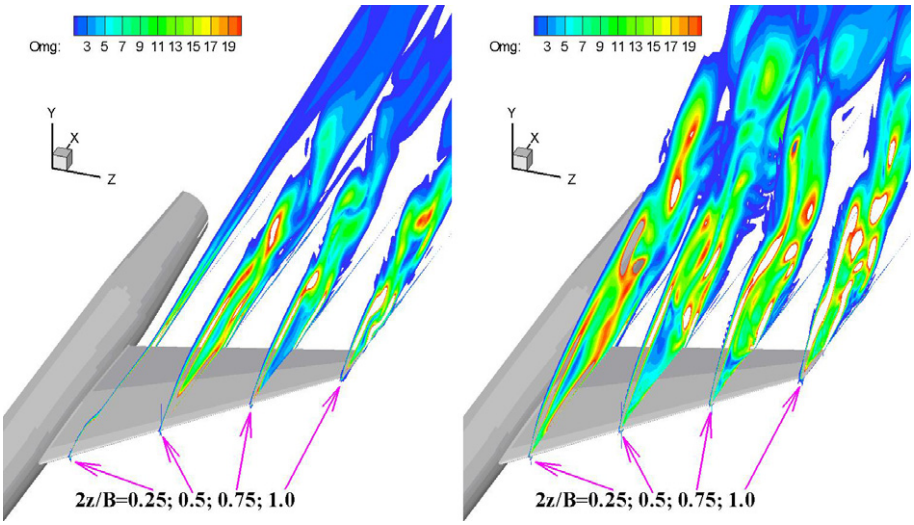

Fig. 14. The instantaneous DDES vorticities over the wing at different AoAs (Left: 12.5°; Right: 26.2°).

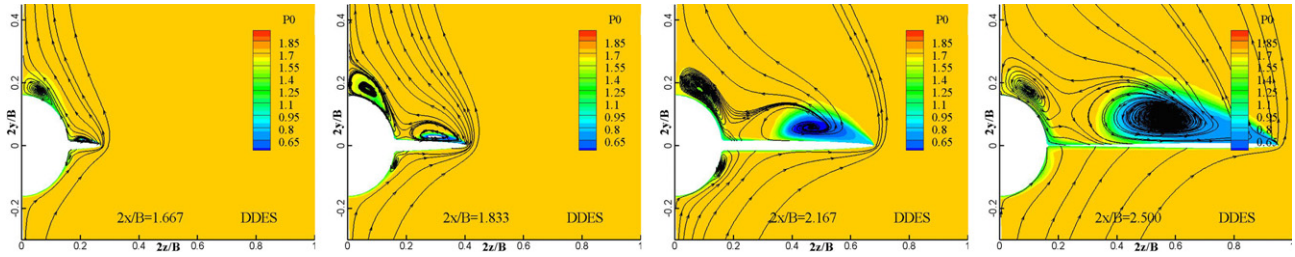

Fig. 15. the transverse flow structure at different streamwise positions by DDES. $2x/B = 1.667$, 1.833, 2.167 and 2.500.

at $2x/B = 2.500$ for the section is located near the root-wing trailing edge.

Fig. 16 presents the transverse flow structures at $2x/B = 2.167$ for RANS, DES and DDES results. The fore-fuse vortex looks very similar while the one from DES is relatively smaller than the other two. As is just discussed, the wing vortex from RANS has not yet broken-down there while breakdown has already taken place with DES and DDES. Thus, the RANS presents a smaller range of total pressure loss with a very strong and concentrated wing vortex. The DES and DDES show that the wing vortex is dispersed with a relatively large total pressure loss region. The surface tracelines shown in Fig. 17 clearly highlight the presence of the horseshoe vortex due to the interaction

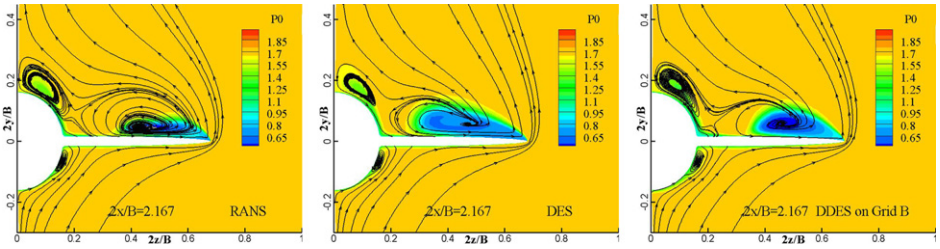

Fig. 16. Comparisons of the flow structures at $2x/B = 2.167$ at the angle of attack of 12.5°. The background color represents total pressure levels.

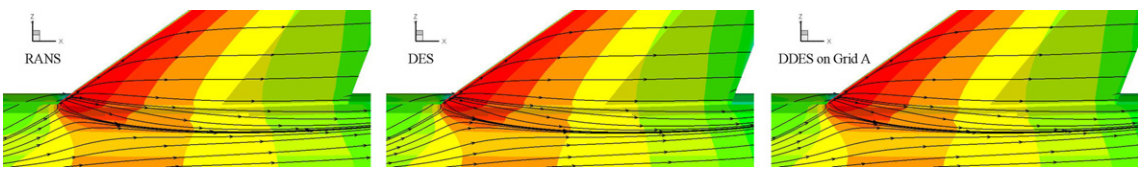

Fig. 17. Comparisons of the lower surface tracelines. The background color represents pressure levels.

between the fuselage and wing that is a typical feature in the wing-body junction flows. All the results indicate the separation line of the horseshow vortex on the lower body surface.

5. Conclusion

This work presents a numerical study of wing-body junction flows with RANS/LES hybrid models. Two typical cases, the Rood wing-body junction and NASA TN D-712 at the angle of attack of 12.5°, have been studied with a RANS (WD+), DES and DDES models in detail. It is observed that the weakly nonlinear correction k–ω model (WD+) can effectively predict the flows past wing-body junctions with adverse pressure gradients at zero and middle angle of attack. But one has to go to DDES to capture the large eddies detached from the leading edge of the wing in NASA TN D-712 case at 12.5° angle of attack. DES delivers the primary horseshoe vortex for the Rood case and the vortex breakdown for the TN D-712 case too far upstream as compared to the measurements. Among the models studied here DDES provides a reliable tool in the modeling of the wing-body junction flows.

Acknowledgement

This project is supported by National Science Foundation of China under Contract 10502030 and 90505005.

References

Apsley, D.D., Leschziner, M.A., 2001. Investigation of advanced turbulence models for the flow in a generic wing-body junction. Flow Turbul. Combust. 67, 25–55.

Chen, H.C., 1995. Assessment of a Reynolds stress closure model for appendage-hull junction flows. J. Fluid. Eng. 117, 557–563.

Devenport, W.J., Simpson, R.L., 1990. Time-dependent and time-averaged turbulence structure near the nose of a wing-body junction. J. Fluid Mech. 210, 23–55.

Durbin, P.A., 1996. On the k–ε stagnation point anomaly. Int. J. Heat Fluid Flow 17, 89–90.

Franke, M., Wallin, S., Thiele, F., 2005. Assessment of explicit algebraic Reynolds-stress turbulence models in aerodynamic computations. Aerospace Sci. Technol. 9, 573–581.

Fu, S., Rung, T., Thiele, F., 1997a. Realizability of the nonlinear stress–strain relationships for Reynolds-stress closure, Turbul. Shear Flows, Vol. 11. Grenoble, France.

Fu, S., Zhai, Z.Q., Rung, T., Thiele, F., 1997b. Numerical study of flow past a wing-body junction with a realizable nonlinear EVM. In: 11th Symposium on Turbulence Shear Flows, Vol. 1. Grenoble, France.

Jones, D.A., Clarke, D.B., 2005. Simulation of a wing-body junction experiment using the Fluent code. In: DSTO-TR-1731.

Menter, F.R., 1994. Two equation eddy-viscosity turbulence models for engineering applications. AIAA J. 32, 1598–1605.

Menter, F.R., Kuntz, M., 2003. A zonal SST-DES formulation. In: DES-WORKSHOP, St. Petersburg.

Parneix, S., Durbin, P.A., Behnia, M., 1998. Computation of 3-D turbulent boundary layers using the V2F model. Flow Turbul. Combust. 60, 19–46.

Roe, P.L., 1981. Approximate Riemann solver, parameter vectors, and difference schemes. J. Comput. Phys. 43, 357–372.

Radespiel, R., Swanson, R.C., 1991. Progress with multi-grid schemes for hypersonic flow problems. In: NASA Tech. Report CR-189579.

Simpson, R.L., 2001. Junction flows. Annu. Rev. Fluid Mech. 33, 415–443.

Soo, H.P., Jang, H.K., 2004. Implementation of k–ω turbulence models in an implicit multigrid method. AIAA J. 42, 1348–1357.

Spalart, P.R., Allmaras, S.R., 1992. A one-equation turbulence model for aerodynamic flows. In: AIAA paper 92-0439, Jan. 1992.

Spalart, P.R., Jou, W.-H., Strelets, M., Allmaras, S., 1997. Comments on the feasibility of LES for wings and on the hybrid RANS/LES approach. In: Advances in DNS/LES, First AFOSR International Conference on DNS/LES, Greden Press.

Sparlart, P.R., Deck, S., Shur, M.L., Squires, K.D., Strelets, M.Kh., Travin, A., 2006. A new version of detached eddy simulation, resistant to ambiguous grid densities. Thero. Comput. Fluid Dyn. 20, 181–195.

Strelets, M., 2001. Detached eddy simulation of massively separated flows. In: AIAA paper 2001-0879.

Wilcox, D.C., 1988. Reassessment of the scale-determining equation for advanced turbulence models. AIAA J. 26, 1299–1310.

Xiao, Z.X., Chen, H.X., Fu, S., Li, F.W., 2005. Computations with k–g model for complex configurations at high-incidence. AIAA J. Aircraft 42, 462–468.

Xiao, Z.X., Chen, H.X., Zhang, Y.F., Huang, J.B., Fu, S., 2006. Study of delayed-detached eddy simulation with weakly nonlinear turbulence model. AIAA J. Aircraft 43, 1377–1385.

Yoon, S., Jameson, A., 1987. Lower–upper symmetric-gauss-seidel method for the Euler and Navier-Stokes equations. In: AIAA paper 1987-0600.